Journal of
Materials Chemistry A

This article can be cited before page numbers have been issued, to do this please use: S. Yi, J. Yan and Q. Jiang, *J. Mater. Chem. A*, 2018, DOI: 10.1039/C8TA01908H.

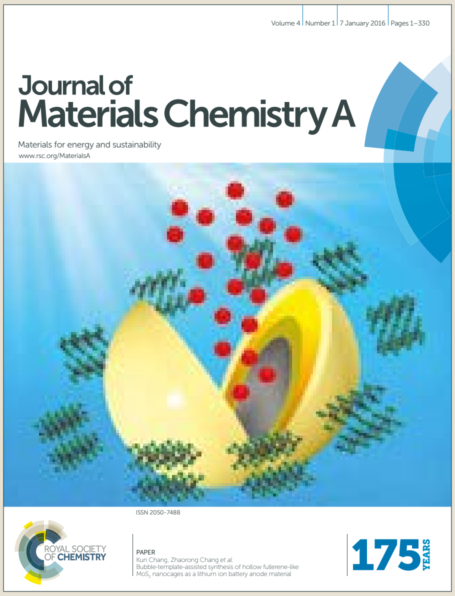

ROYAL SOCIETY
OF CHEMISTRY

rsc.li/materials-a

View Article Online
DOI: 10.1039/C8TA01908H

Journal of Materials Chemistry A

PAPER

Carbon quantum dots sensitized integrated Fe_2O_3@g-C_3N_4 core-shell nanoarrays photoanode towards highly efficient water oxidation

Received 00th January 20xx,
Accepted 00th January 20xx

DOI: 10.1039/x0xx00000x

www.rsc.org/

Sha-Sha Yi, Jun-Min Yan, and Qing Jiang*

Constructing integrated heterojuction system photoelectrodes for solar energy conversion is indubitable to be an efficient alternative method due to their effectiveness in charge separation and optimizing the ability for reduction and oxidation reactions. Here, an integrated photoanode constructed by carbon quantum dots (CQDs) sensitized Ti:Fe_2O_3@GCNNs (where GCNNs represents graphitic carbon nitride nanosheets) core-shell nanoarrays are demonstrated, showing a smart photocurrent density as high as 3.38 mA cm^{-2} at 1.23 V versus reversible hydrogen electrode (V_{RHE}), 2-fold higher than that of the pristine Ti:Fe_2O_3, which is superior over that of recently reported promising photoanodes (Table S1). In this ternary system (Ti:Fe_2O_3@GCNNs-CQDs), each of which plays a specific role in the process for superior PEC water oxidation that i) the vectorial holes transfer of Ti:Fe_2O_3 $\rightarrow$ g-C_3N_4 $\rightarrow$ CQDs; ii) the introduction of CQDs has high catalytic activity for H_2O_2 decomposition contributing high rate activity for water oxidation via a two-step-two-electron water-splitting process; iii) the favorable electron transport behaviors of CQDs. This controlled structure designing represents one scalable alternative toward the development of photoanode for high-efficiency water splitting.

Introduction

During natural photosynthesis, photosystem II (PS II) and photosystem I (PS I) capture light energy to generate photoexcited photons for participating water oxidation and reduction of coenzyme called ferredoxinnicotinamide adenine dinucleotide phosphate (NADP) on two photosystems individually, which a process is achieved and connected in series with an electron transfer chain.[1-3] In such a careful arrangement of photosynthetic constituent, the two photosynthetic reactions (reduction and oxidation reactions) take place simultaneously in time but separately in space, thus addressing the high quantum efficiency derived from the efficient charge separation in spatial.[2] Inspired by this natural photosynthesis, photoelectrochemical (PEC) water splitting based heterojunction artificial photosynthesis for chemical fuel is so fascinating, that it is a promising solution to critical problems facing the modern industrial development including of unrenewable energy sources, environmental pollution as well as the issues of effective storage and transport.[4-6] Much research based on various photoanodes materials, such as TiO_2, Fe_2O_3, $BiVO_4$, WO_3[7-10] *et al*, have been devoted to achieving high PEC performance. Especially Fe_2O_3, it has emerged and gained considerable attention as a model material for PEC water splitting due to the good sunlight-harvesting capability with the desirable band gap of ~1.9-2.2 eV,[7] more positive potential of its valence band (VB) than E°(O_2/H_2O)),[11] excellent stability as well as natural abundance.[12] However, pure Fe_2O_3 limits low energy conversion efficiency with poor charge transport and slow rapid carrier collection properties that prevents efficient charge separation in bulk and surface.[13] Thus, it is highly desired to build of a heterojunction photoelectrode for water oxidation to overcome this challenges, a structure that the high separation of charge carriers as well as the fast water oxidation kinetics can be achieved simultaneously.

On this concept, we attempt to construct the well and integrated heterojunction photoanode for PEC water oxidation, which consists of titanium-doped hematite (Ti:Fe_2O_3) nanoarrays, graphitic carbon nitride nanosheets (GCNNs), and ultra-small carbon quantum dots (CQDs). In this system, Ti is doped as a foreigner in Fe_2O_3 to effectively boost the bulk charge separation by adjusting the band-bending.[14] Recently, graphitic carbon nitride (g-C_3N_4) has received great attention for direct photocatalytic water splitting on account of its appropriate bandgap (~ 2.7 eV) and high stability.[15] Moreover, GCNNs shows much higher negative conduction band (CB) and lower VB potentials as compared to bulk g-C_3N_4 because of its quantum confinement effect.[16] Thus imagine that GCNNs can be introduced as a second semiconductor with Ti:Fe_2O_3 to form heterojuction photoanode for superior water oxidation, which is not reported so far. Furthermore, it is reported that CQDs can boost charge carriers separation as well as shift the onset potential of the photoelectrode, resulting in a higher photocurrent density.[17] On the other hand, *Kang* et al[18] have confirmed that the CQDs possess high catalytic activity for H_2O_2 decomposition on photocatalytic process

---

Key Laboratory of Automobile Materials (Jilin University), Ministry of Education, Department of Materials Science and Engineering, Jilin University, Changchun, 130022, China.
E-mail: junminyan@jlu.edu.cn

Electronic Supplementary Information (ESI) available. See DOI: 10.1039/x0xx00000x

View Article Online
DOI: 10.1039/C8TA01908H

of $g\text{-}C_3N_4$, then we imagine that their combination can also be applied to the PEC process.

In this paper we implement the concept of natural photosynthesis using $Ti:Fe_2O_3$ nanoarrays as the core and GCNNs as the shell to form core-shell structure photoanode for PEC water splitting through a facile step-by-step route. To extract the best possible performance of $Ti:Fe_2O_3$, CQDs is selected as the sensitizer owing to its high catalytic activity for H_2O_2 decomposition as well as the favorable electron transport behaviors. As results, the ultimate $Ti:Fe_2O_3$@GCNNs-CQDs photoanode exhibits surprising high photocurrent density (3.38 mA cm^{-2} at 1.23 V_{RHE}) and efficiency with respect to $Ti:Fe_2O_3$. The underlying mechanism is systematic studied and the results show that each of which plays a specific role in the process for superior PEC water oxidation.

Results and discussion

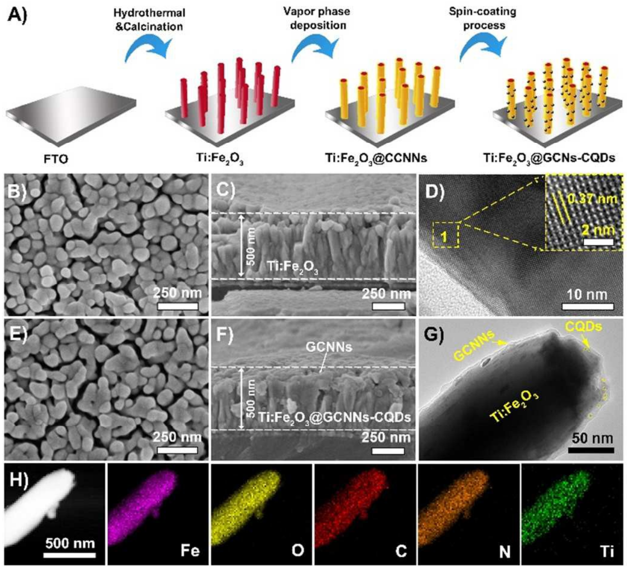

Fig. 1 (A) Scheme illustration for the preparation of $Ti:Fe_2O_3$@GCNNs-CQDs nanoarrays. (B) Top-view and (C) cross-sectional-view FESEM images of $Ti:Fe_2O_3$. (D) HRTEM images of $Ti:Fe_2O_3$. (E) Top-view, (F) cross-sectional-view FESEM images, and (G) TEM image of $Ti:Fe_2O_3$@GCNNs-CQDs. (H) STEM-EDX element mapping for $Ti:Fe_2O_3$@GCNNs-CQDs.

As illustrated in Fig. S1A, the transmission electron microscopy (TEM) image of the carbon quantum dots (CQDs) product shows its morphology of ultra-small particles with a diameter of 1.70 nm. In Fig. S1B, the combination of clear peaks at 1379 cm^{-1} (D-bond) and 1593 cm^{-1} (G-bond) for Raman spectrum of pristine CQDs are easily observed.[19] To explore the electronic structure and optical properties of CQDs, the ultraviolet-visible diffuse reflectance spectra (UV-vis DRS) and photoluminescence (PL) emission spectra are performed. As shown in Fig. S1C, CQDs demonstrates its intrinsic light absorption edge of 550 nm with the energy band gap (E_g) of 2.22 eV, based on the Kubelka-Munk method.[20] Fig. S1D records the PL spectra of CQDs with the excitation wavelengths range from 300 to 500 nm, showing that the centered wavelength of the emission peak shifts to higher values as the excitation wavelength increased, which probably originates from the characteristic of CQDs itself, deriving from its surface defect emission.[21] In addition, graphitic carbon nitride ($g\text{-}C_3N_4$) demonstrates its morphology of ultra-thin nanosheets (Fig. S2), denoted as GCNNs. Furthermore, Fig. S3 compares the UV-vis DRS and PL emission spectra of GCNNs and bulk $g\text{-}C_3N_4$, and the results indicate that the blue-shifted E_g and PL spectra for GCNNs can be ascribed to the quantum confinement effect with the conduction band (CB) and valence band (VB) shifting in opposite directions.[16,22]

The preparation process of $Ti:Fe_2O_3$@GCNNs-CQDs photoanode is demonstrated in Fig. 1A. Clearly, Ti-doped Fe_2O_3 ($Ti:Fe_2O_3$) nanoarrays are primarily fabricated on fluorine-doped tin oxide (FTO) via a simple calcination-assisted hydrothermal approach. Then, dicyandiamide is chosen as the precursor of GCNNs grown on $Ti:Fe_2O_3$ by method of vapour phase deposition method in furnace in air at 550℃ for 3 h to obtain the integrated $Ti:Fe_2O_3$@GCNNs core-shell structure. Finally, the sensitization of CQDs is conducted using a simple spin-coating strategy followed by drying at 100℃ overnight. In this way, the well-controlled CQDs sensitized integrated $Ti:Fe_2O_3$@GCNNs core-shell nanoarrays are successfully synthesized. Similarly, $Ti:Fe_2O_3$@GCNNs and $Ti:Fe_2O_3$/CQDs can also be obtained by the method above except for the processes of CQDs sensitization and GCNNs spin-coating process, respectively. In Figs. 1B and 1C, the typical field-emission scanning electron microscopy (FESEM) of the top-view and cross-sectional-view images of $Ti:Fe_2O_3$ demonstrate its morphology of nanoarrays made up of numerous nanorods, which diameter and length are ~100 and 500 nm, respectively. The HRTEM image reveals the growth direction of the Fe_2O_3 nanorod along (104) with the lattice fringes of 0.37 nm (Fig. 1D), furthermore, Fe_2O_3 shows its single crystalline nature (Fig. S4). In addition the dual loading of GCNNs and CQDs on $Ti:Fe_2O_3$, the frame structure of the compound photoelectrode is highly maintained dues to the thin layers of GCNNs together with the ultra-small of CQDs (Figs. 1E and 1F). Furthermore, the TEM image of $Ti:Fe_2O_3$@GCNNs-CQDs is performed for much clearly to see its structure, showing that GCNNs nanolayers with thin thickness are coated on the surface of $Ti:Fe_2O_3$ to form the integrated core-shell hybrid; CQDs are firmly and uniformly deposit on the surface of GCNNs layers (Figs. 1G and S5). By comparing the selected area electron diffraction (SAED) images of $Ti:Fe_2O_3$ and $Ti:Fe_2O_3$@GCNNs-CQDs (Fig. S4), we confirm the co-existence of $Ti:Fe_2O_3$ and GCNNs in the later. Further observation by the elemental mapping images obtained by scanning TEM-energy-dispersive X-ray (STEM-EDX) are demonstrated in Fig. 1H, showing the presence of Fe, O, C, N, and Ti elements, and imply that GCNNs layers are uniformly coated on the $Ti:Fe_2O_3$ nanorods surface.

To investigate the structural, composition and interaction in modified $Ti:Fe_2O_3$ specimens, X-ray diffraction (XRD), Raman, and X-ray photoelectron spectroscopy (XPS) techniques are systematically investigated. The XRD patterns of the obtained four photoanodes are presented in Fig. 2A, except for the peaks of Fe_2O_3[23] and SnO_2 (be from FTO substrate), there is no characteristic peaks corresponding to GCNNs and CQDs. In Fig. 3B, the intrinsic Raman bands of Fe_2O_3 peaking at 222, 242, 286, 440, 496, 608, and 1316 cm^{-1} are found for the $Ti:Fe_2O_3$ based four photoanodes.[24] For specimens of $Ti:Fe_2O_3$/CQDs and $Ti:Fe_2O_3$@GCNNs-CQDs, there appears characteristic peak corresponding to CQDs, locating at

View Article Online
DOI: 10.1039/C8TA01908H

1595 cm^{-1} (Fig. S1B). While there is no Raman peak for GCNNs, during that the laser wavelength of 532 nm cannot make it excited. It is interest to observe that the slightly changing of Raman shift at 222 cm^{-1} is found for modified Ti:Fe_2O_3-based three photoanodes in comparison with the Ti:Fe_2O_3 (Fig. S6), powerfully suggesting that the strong interactions among GCNNs, CQDs andTi:Fe_2O_3 leads to an increased probability of charge exchange and transfer among them[25] for high separation of photogenerated charge carriers in PEC water oxidation. Moreover, the Raman signal at 660 cm^{-1} can only be found for Ti:Fe_2O_3 (Fig. S7), which manifests the incorporation of Ti atoms into the Fe_2O_3, ascribing to the disorder-sensitive mode generated by the Ti^{4+} dopant incorporation.[24,26] Fig. 2C-F shows the XPS spectra of Fe 2p, O 1s, C 1s, and N 1s, respectively, for Ti:Fe_2O_3@GCNNs-CQDs specimen. The Fe 2p detailed high-resolution XPS spectra is shown in Fig. 2C, and the Fe $2p_{1/2}$ and Fe $2p_{3/2}$ binding energies (BEs) of 724.5 and 710.7 eV are fully consistent with typical values reported for Fe_2O_3.[27] In addition, the BEs of 713.5 and 709.7 eV together with the satellite peak of Fe $2p_{3/2,sat}$ centered at 717.6eV are all characteristics of Fe^{3+}.[28,29] Fig. 2D illustrates the O 1s spectrum region, which can be decomposed into three well-fitted peaks locating at 530.1, 531.2 and 533.1 eV, can be assigned to Fe-O, O-H, and O=C-O* groups, respectively.[30-32] Notably, the pronounced shoulder for O-H group in Ti:Fe_2O_3@GCNNs-CQDs (Fig. 2D) compared with Ti:Fe_2O_3 (Fig. S8) together with the O=C-O* group indicates the existence of CQDs in this composite photoelectrode.[31] Besides, it is worth mentioning that the Fe 2p and O 1s spectra for Ti:Fe_2O_3@GCNNs-CQDs show slightly the increasing BEs than that of Ti:Fe_2O_3 (Fig. S8), indubitably manifesting the interaction among CQDs, GCNNs and Ti:Fe_2O_3. Fig. 2E shows the high-resolution XPS C 1s spectra, it can be clearly seen that three peaks with BEs at 284.6, 286.1, and 288.0 eV are observed, corresponding to theC-C, C-O in CQDs[21] (or C-N in GCNNs),[15] and C=O in CQDs[16] (or N-C=N in GCNNs),[15] respectively. In the region of N 1s spectrum (Fig. 2F), three strong peaks with their BEs at 398.5, 399.7, and 400.6 eV, respectively, attributed to the pyridinic nitrogen (C-N=C), pyrrolic nitrogen (C-N-C), and quaternary nitrogen (N-$(C)_3$) of GCNNs[16,33] can be observed, which means that the modified Ti:Fe_2O_3 contains the component of GCNNs. The Ti 2p XPS spectrum recorded in Fig. S9 suggests that Ti exists in the form of Ti^{4+}.[34] In summary, these results prove that the Ti:Fe_2O_3@GCNNs-CQDs photoanode is indeed successfully synthesized.

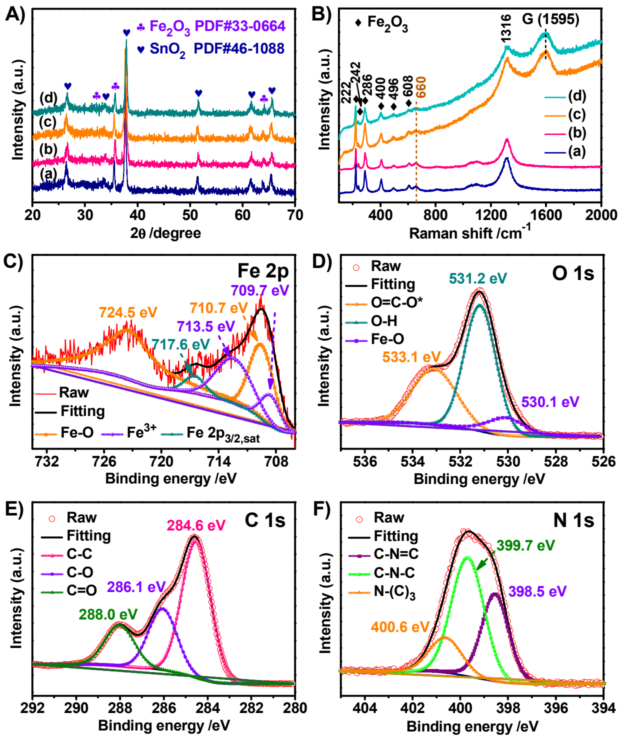

Fig. 2 (A) XRD patterns and (B) Raman spectra of (a) Ti:Fe_2O_3, (b) Ti:Fe_2O_3@GCNNs, (c) Ti:Fe_2O_3/CQDs, and (d) Ti:Fe_2O_3@GCNNs-CQDs specimens. XPS spectra of (A) Fe 2p, (B) O 1s, (C) C 1s, and (D) N 1s for Ti:Fe_2O_3@GCNNs-CQDs photoelectrode.

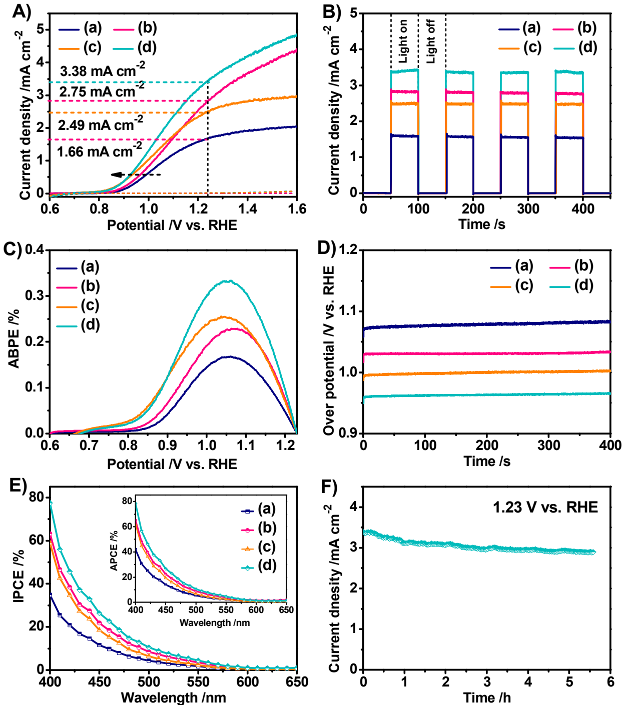

Fig. 3 Solar-light-driven PEC performances of (a) Ti:Fe_2O_3, (b) Ti:Fe_2O_3@GCNNs, (c) Ti:Fe_2O_3/CQDs, and (d) Ti:Fe_2O_3@GCNNs-CQDs photoanodes, respectively, for water oxidation in 1 M KOH at pH 13.6: (A) LSV plots recorded under AM 1.5G illumination, 100 mW cm^{-2} (dark currents are shown in the dash lines); (B) *I-t* curves at 1.23 V_{RHE}; (C) ABPE spectra; (D) potential (V_{RHE}) versus time for photoelectrodes, at 1 mA cm^{-2}; (E) IPCE spectra obtained at 1.23 V_{RHE} (inset: APCE spectra). (F) Long-time stability test recorded on 1.23 V_{RHE} under AM 1.5G illumination for Ti:Fe_2O_3@GCNNs-CQDs photoanode.

To evaluate how the modification of CQDs and GCNNs affect the PEC water-oxidation of our Fe_2O_3 photoelectrodes, we perform systematically their performances in a typical three-electrode cell using a simulated solar light (AM 1.5G). In our study, Ti:Fe_2O_3 is employed as a model photoanode, for that the Ti-dopant can effectively boosts the charge separation by reason of anodic-shifted

View Article Online
DOI: 10.1039/C8TA01908H

flat band potential (E_{fb}) (Fig. S10) that can boost band-bending,[14] resulting in significant performance improvement of photocurrent density. As a result, the 0.5 at.% Ti dopant Fe_2O_3 (labelled as Ti:Fe_2O_3) bring out the maximum current density of 1.66 mA cm^{-2} at 1.23 V_{RHE} (versus reversible hydrogen electrode) (Fig. S11). To gain the higher PEC behaviour, we optimize the Ti:Fe_2O_3 through controlled experiments by comparing the loading amounts of GCNNs (Fig. S12) and CQDs (Fig. S13), respectively. Notably, the optimized Ti:Fe_2O_3@GCNNs and Ti:Fe_2O_3/CQDs show much enhanced photocurrent densities of 2.75 and 2.49 mA cm^{-2} at 1.23 V_{RHE}, respectively, as compared with Ti:Fe_2O_3. Significantly, the linear sweep voltammetry (LSV) plot in Fig. 3A reveals that Ti:Fe_2O_3@GCNNs-CQDs exhibits an prominent photocurrent density of 3.38 mA cm^{-2} at the same potential, which is two and about eight times higher than that of Ti:Fe_2O_3 and Fe_2O_3 (Fig. S11), respectively. These results confirm that our fabricated hybrid structure in favor of charge separation and transportation for PEC water-oxidation (vide-infra), with their results are comparable to the high performance of hematite reported recently (Table S1). Notably, an apparent cathodic shift on onset potentials observed for both specimens of Ti:Fe_2O_3/CQDs and Ti:Fe_2O_3@GCNNs-CQDs, shifting ca. 70 mV_{RHE} which can be much more apparently seen in spectrum of first-order derivative of the photocurrent density as a function of voltage[35] (Fig. S14). The above phenomena shed light on that the CQDs can perfect the kinetic of Fe_2O_3 for water oxidation. Moreover, the steady state photocurrent based on amperometric *I-t* curves at 1.23 V_{RHE} (Fig. 3B) together with the transient photocurrent responses under chopped light (Fig. S15) are further conducted to analyse the photocurrent density improvement by incorporation of CQDs and GCNNs. Gratifyingly, these results are in high accordance with the LSV results.

Furthermore, an analysis of the applied bias photon-to-current efficiency (ABPE) characteristics derived from the LSV plots show that the composite electrode configuration (Ti:Fe_2O_3@GCNNs-CQDs) shows its ABPE value of 0.33%, which is much higher than the values obtained for all the other three photoanodes (Fig. 3C). To evaluate how the extent of coupling of GCNNs and CQDs affects the over potential of the Ti:Fe_2O_3 photoanode, we compare the potentials by providing the same current density (1 mA cm^{-2}) for each photoelectrode (Fig. 3D), which is a measurement for characterizing their charge separation and transportation behaviours. As results, the over potential decreases in the order of Ti:Fe_2O_3 < Ti:Fe_2O_3@GCNNs < Ti:Fe_2O_3/CQDs < Ti:Fe_2O_3@GCNNs-CQDs, with their values of 1.07, 1.03, 0.99, and 0.96 V_{RHE}, respectively. To further identify our well-designed hybrid structure, the incident photon-to-current efficiency (IPCE) and absorbed photon-to-current efficiency (APCE) spectra are also conducted under PEC water-oxidation conditions. These constructed Ti:Fe_2O_3@GCNNs-CQDs hybrid photoanode is optimized to exhibit both the high IPCE and APCE values in the wavelength range from 400 to 650 nm compared to that of Ti:Fe_2O_3 (Fig. 3E), which is consistent with the LSV plots. The maximum IPCEs are achieved at 400 nm, which are 34.8, 63.2, 58.8, and 77.4% for Ti:Fe_2O_3, Ti:Fe_2O_3@GCNNs, Ti:Fe_2O_3/CQDs, and Ti:Fe_2O_3@GCNNs-CQDs, respectively. In a word, the enhanced PEC water-oxidation performances of Ti:Fe_2O_3@GCNNs-CQDs are expected to be assigned to the reasons of the enhanced charge separation, the boosted water-oxidation kinetics as well as the fast electrons transport owning to its high conductivity. The long-term current density versus time (*I-t*) performance for Ti:Fe_2O_3@GCNNs-CQDs is conducted (Fig. 3F); the current density is well matched with the LSV result, with highly stable behavior for more than 5 h.

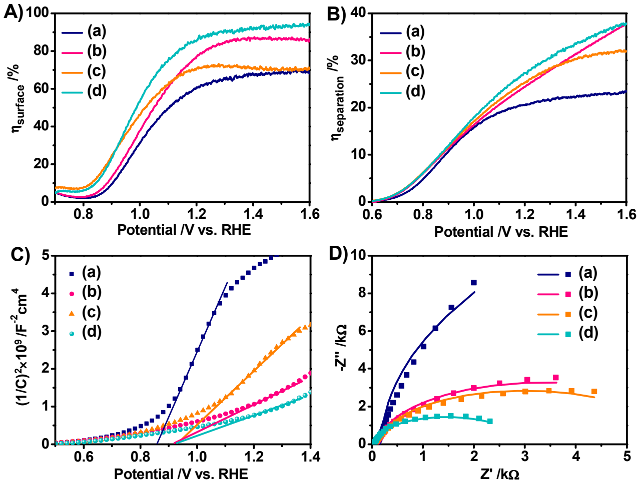

Fig. 4 (A) Surface charge injection efficiency, (B) bulk charge separation efficiency, (C) M-S plots collected at a frequency of 1 kHz in dark, and (D) EIS Nyquist plots under AM 1.5G illumination for based Ti:Fe_2O_3 photoanodes of (a) Ti:Fe_2O_3, (b) Ti:Fe_2O_3@GCNNs, (c) Ti:Fe_2O_3/CQDs, and (d) Ti:Fe_2O_3@GCNNs-CQDs, respectively.

To gain insights into the effect of surface coupling of CQDs and GCNNs on enhancement of photocurrent density of Ti:Fe_2O_3, the surface charge injection efficiency ($\eta_{injection}$) and bulk charge separation efficiency ($\eta_{separation}$) are also carried out by a comparison study between J_{H2O} and J_{SO3}^{2-} (the photocurrent density achieved by oxidation of H_2O and Na_2SO_3) as well as the theory current density (J_{abs}), a product of the AM 1.5G spectrum and the light harvesting efficiency (LHE) of the photoelectrode. The comparison of the J_{H2O} and J_{SO3}^{2-} for each photoanode, the LHE together with the J_{abs} are shown in Figs. S16 and S17. As results, the $\eta_{injection}$ and $\eta_{separation}$ are plotted in Figs. 4A and 4B, respectively, and the well-constructed Ti:Fe_2O_3@GCNNs-CQDs hybrid photoanode can able to reach $\eta_{injection}$ of 87.3% at 1.23 V_{RHE}, which is much higher than those of Ti:Fe_2O_3 (62.4%), Ti:Fe_2O_3@GCNNs (80.0%), and Ti:Fe_2O_3/CQDs (71.9%), respectively. The observed enhancement of $\eta_{injection}$ for Ti:Fe_2O_3@GCNNs and Ti:Fe_2O_3/CQDs suggests that the GCNNs and CQDs can augment the separation of photogenerated electron-hole pairs, illuminating that more holes can arrive the electrode/electrolyte interface for participating the PEC water oxidation reaction, compared to Ti:Fe_2O_3 electrode. Furthermore, the above tendency is also observed for $\eta_{separation}$ at 1.23 V_{RHE} for Ti:Fe_2O_3@GCNNs-CQDs with respect to Ti:Fe_2O_3 (Fig. 4B), Ti:Fe_2O_3@GCNNs, and Ti:Fe_2O_3/CQDs, with their $\eta_{separation}$ values to be 28.5, 21.0, 25.5, and 26.4%, respectively. These results indicate that the formed heterojunction in Ti:Fe_2O_3@GCNNs-CQDs hybrid can control the charges behavior, which can facilitate the electron-hole pairs separation in bulk of Ti:Fe_2O_3.[36]

View Article Online
DOI: 10.1039/C8TA01908H

To further discuss the effect of GCNNs and CQDs on the electrical properties of Ti:Fe_2O_3, Mott-Schottky (M-S) plots and electrochemical impedance spectroscopy (EIS) measurements are conducted on the photoelectrodes. Fig. 4C compares the M-S plots of Ti:Fe_2O_3-based four photoelectrodes in dark condition with 1 kHz frequency in 1 M KOH, revealing that all the photoelectrodes show the positive slope, indicating their n-type semiconductor nature. The charge carrier density, N_D, is derived from the slope of the M-S plots, producing values of 1.3×10^{20}, 5.8×10^{20}, 3.0×10^{20}, and 68.7×10^{20} cm^{-3} for Ti:Fe_2O_3, Ti:Fe_2O_3@GCNNs, Ti:Fe_2O_3/CQDs, and Ti:Fe_2O_3@GCNNs-CQDs, respectively. This suggests that loading of CQDs and GCNNs can increase donor density of Ti:Fe_2O_3 independently, and a further higher donor density is achieved by coupling of them simultaneously due to better charge separation and transport which inhibits bulk/surface recombination.[37] By extrapolating the M-S plots to the x-axis (i.e., $1/C^2 = 0$) to achieve the intercept, that the value represents the E_{fb} of a photoelectrode. Clearly, in comparison with the Ti:Fe_2O_3 specimen, the other three Ti:Fe_2O_3-based hybrid photoanodes exhibit an positive shift of E_{fb}, which suggests that the composite photoanodes have decreased band bending, which is beneficial to the facilitated electrode/electrolyte interface charge transfer as well as the increased semiconductor/electrolyte interface.[8,9]

In Fig. 4D, EIS technique is conducted under an open circuit potential (OCP) condition and AM 1.5G irradiation, which can used to expound the charge separation and transportation process in this photoanodes. The equivalent circuit shown in Fig. S18 is used for fitting the EIS data, in which R_s, R_{trap}, and R_{ct} express as the series resistance at the interface between the FTO substrate and bulk Ti:Fe_2O_3, the bulk charge trapping resistance, as well as the surface charge transfer resistance at the photoelectrode/electrolyte interface,[37,38] respectively, with their fitting results listed in Table S2. It can be clearly seen that the R_s is found dramatically decreased with loading GCNNs and CQDs on Ti:Fe_2O_3 in sequence with respect to pristine Ti:Fe_2O_3, which suggests that the electron leakage case on exposed FTO is well protected.[39] Moreover, the R_{trap} for Ti:Fe_2O_3@GCNNs-CQDs is 30 Ω which is much smaller than that of Ti:Fe_2O_3 (589 Ω), because of the effective surface coupling by GCNNs and CQDs, indicating the high efficiency of formed heterojunction for water oxidation.[37] Meanwhile, it is also notable that a smallest R_{ct} value for Ti:Fe_2O_3@GCNNs-CQDs is observed relatives to the other photoanodes, suggesting that the charge transfer resistance is dramatically decreased after loading of GCNNs and CQDs dues to their favorable electron transport behaviors, a significant process for higher PEC performance owing the fast charge transfer characteristic.

To gain in-depth insight into the superior PEC performance of water oxidation, the comparison rate of H_2 or O_2 generation on Ti:Fe_2O_3 and Ti:Fe_2O_3@GCNNs-CQDs photoanode at 1.23 V_{RHE} under AM 1.5G illumination is demonstrated in Fig. 5. The O_2 generation rate on Ti:Fe_2O_3@GCNNs-CQDs photoanode is found to be 2-fold larger than that of Ti:Fe_2O_3, corresponding to 27.0 and 11.9 μmol h^{-1}, respectively. The faradaic efficiencies (η) of O_2 generation for Ti:Fe_2O_3@GCNNs-CQDs and Ti:Fe_2O_3 photoanodes are calculated to be 91.2 and 90.1%, respectively. Note that these η values are slightly lower than expected (100%), which probably due to the gas leak during collection.[40]

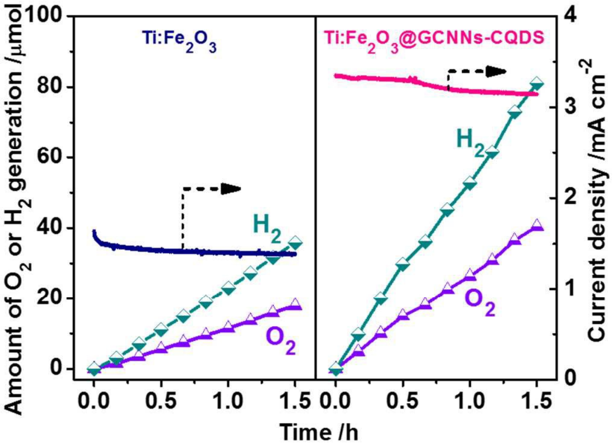

Fig. 5 The generation of H_2 and O_2 with Ti:Fe_2O_3 (left) and Ti:Fe_2O_3@GCNNs-CQDs (right) photoanodes and the concurrent i-t curves at 1.23 V_{RHE} under AM 1.5G illumination.

To achieve highly efficient PEC conversion, the pivotal factor focuses on maximize extracting the photogenerated charge carriers to the surface while impressing their recombination. Therefore, we analyse the energy band positions of each component in Ti:Fe_2O_3@GCNNs-CQDs photoanode, for fully understanding the working mechanism of the transportation of these photogenerated charge carriers. Ti:Fe_2O_3, GCNNs and CQDs demonstrate their optical E_g values of 2.05, 3.05 and 2.22 eV, respectively, as shown respectively in Figs. S19, S3A and S1C. As for Ti:Fe_2O_3 and GCNNs specimens, the E_{fb} values are first performed to estimate their E_{CB} positions base on method of M-S plots, which are -0.15 and -1.39 V *vs*. Ag/AgCl (Figs. S10 and S20), respectively. Because of the small difference between E_{fb} and E_{CB} for n-type semiconductor nature,[41] the E_{CB} potential levels for Ti:Fe_2O_3 and GCNNs are calculated to be 0.05 and -1.19 V *vs*. NHE,[10] respectively. Additionally, according to the cyclic voltammetry (CV) curve in Fig. S21, the LUMO level of CQDs can be estimated to be -0.83 V *vs*. Ag/AgCl, that is -0.63 V *vs*. NHE. Thus, the E_{VB} (or HOMO) level for Ti:Fe_2O_3, GCNNs and CQDs are reckon up to be 2.1, 1.86 and 1.59 V *vs*. NHE, respectively, by equation of $E_{VB} = E_{CB} + E_g$.[41] To observe clearly the E_g, E_{CB} (or LUMO) and E_{VB} (or HOMO) of Ti:Fe_2O_3, GCNNs and CQDs, their values are summarized in Table S3.

In our LSV results (Fig. 3A), the much enhanced photocurrent density responses of Ti:Fe_2O_3@GCNNs and Ti:Fe_2O_3/CQDs are achieved with respect to Ti:Fe_2O_3, indicates the higher separation efficiency of photogenerated electron-hole pairs in integrated heterojunction system photoanodes (Fig. S22), which can also be proved by the photoluminescence (PL) spectra (Figs. S23 and S24). Furthermore, it is reported that CQDs shows high catalytic activity for H_2O_2 decomposition, an intermediate of PEC water oxidation, which higher reaction rate may be achieved in this process.[18,27] As state above, the proposed schematic diagram illustrating the mechanism of Ti:Fe_2O_3@GCNNs-CQDs for PEC water splitting is given in Scheme 1. Under AM 1.5G illumination, photogenerated electron-hole pairs are firstly obtained respectively in specimens of Ti:Fe_2O_3, GCNNs and CQDs. Clearly, VB-holes of Ti:Fe_2O_3 can rapidly transfer to VB-holes of GCNNs, and subsequently to VB of CQDs;

View Article Online
DOI: 10.1039/C8TA01908H

then the VB-holes of CQDs could contribute to a high rate activity for water oxidation by the stepwise two-electron/two-electron process: (i) $2H_2O \rightarrow H_2O_2 + H_2$; (ii) $2H_2O_2 \rightarrow 2H_2O + O_2$.[18] To confirm this suppose, LSV plots based on CQDs integrated photoanodes are performed in 0.05 M (pH = 7.0) phosphate buffered 25 mM H_2O_2 solution in dark condition (Fig. S25), with its results suggest the fact that CQDs shows indeed the catalytic ability for H_2O_2 decomposition, in agreement with the previous report.[18] At the same time, CB-electrons of GCNNs can be quickly injected to CB of $Ti:Fe_2O_3$, then flow to the FTO substrate, and ultimately to the Pt counter electrode for water reduction. In addition, we find that the CB-electrons of CQDs are leaved, which also can be used for water reduction (Fig. S26), due to the suitable CB level position and high conductivity of CQDs as well as its higher transfer rate of electrons than holes. As such, charge recombination in $Ti:Fe_2O_3$ can be effectively suppressed after introducing of GCNNs and CQDs, and therefore more holes can be released for water oxidation. We therefore attribute the superior PEC performances of our $Ti:Fe_2O_3$@GCNNs-CQDs photoanode to: i) the delicate heterojunction designing for efficient charge separation and transportation; ii) the introduction of CQDs to contribute high rate activity for water oxidation by the stepwise two-electron/two-electron process; iii) the favorable electron transport behaviors of CQDs that boosts charge separation. We are therefore confident that the delicate structure presented herein provide new insight into the design of high PEC systems.

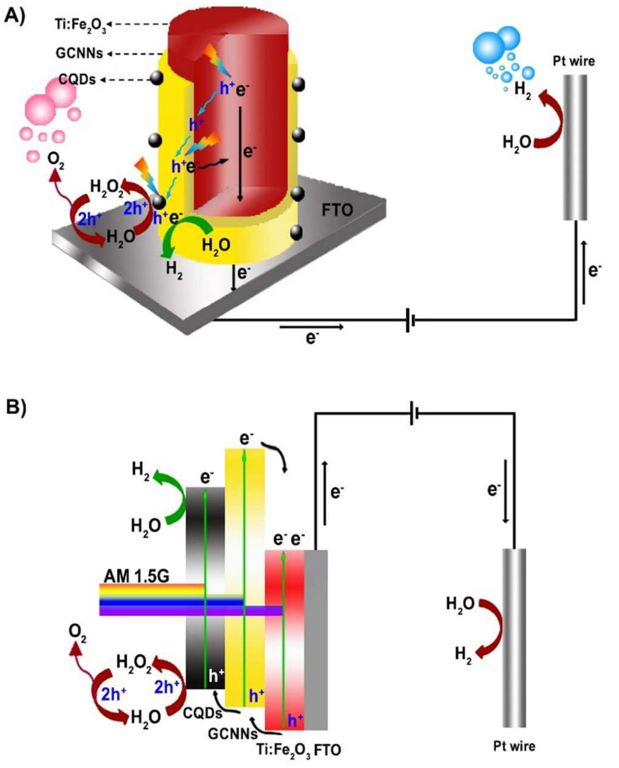

Scheme 1. (A) Schematics of the CQDs modified heterojunction system of $Ti:Fe_2O_3$@GCNNs core-shell heterostructure used for PEC water splitting. (B) The energy band schematic of our heterojunction structure.

Conclusions

In summary, we presented an integrated artificial photosynthesis system of $Ti:Fe_2O_3$@GCNNs-CQDs, which processes smart high photocurrent density, high stability, and efficient surface charge injection and bulk charge separation efficiency. The resulting ternary system shows a water oxidation photocurrent density of 3.38 mA cm^{-2} at 1.23 V_{RHE}, which is 2-fold higher than that of $Ti:Fe_2O_3$ and a comparable value to that of many reported promising photoanodes. There are mainly two factors leading to the highly efficient PEC performance, which is that the greatly enhanced separation of charge carriers at interface of $Ti:Fe_2O_3$@GCNNs deriving from the delicate heterojunction constructed; the high catalytic behaviour of CQDs for H_2O_2 decomposition leading to rapidly oxidized to O_2 through two-step-two-electron reaction partway. Our sunlight-driven PEC water-splitting device paves the way toward to design solar-to-fuel conversion efficiency photoelectrodes with low cost, highly efficient as well as stable.

Conflicts of interest

There are no conflicts to declare.

Acknowledgements

This work is supported in part by the National Natural Science Foundation of China (51522101, 51631004, 51471075, and 51401084); Specialized Research Fund for the Doctoral Program of Higher Education of China (20110061120040); and Program for Innovative Research Team (in Science and Technology) in University of Jilin Province.

Notes and references

1 H. Li, Y. Gao, Y. Zhou, F. Fan, Q. Han, Q. Xu, X. Wang, M. Xiao, C. Li and Z. Zou, *Nano Lett.* 2016, **16**, 5547-5552.
2 Y. Tachibana, L. Vayssieres and J. R. Durrant, *Nat. Photonics* 2012, **6**, 511-518.
3 C. Liu, J. Tang, H. M. Chen, B. Liu and P. Yang, *Nano Lett.* 2013, **13**, 2989-2992.
4 J. Luo, J.-H. Im, M. T. Mayer, M. Schreier, M. K. Nazeeruddin, N.-G. Park, S. D. Tilley, H. J. Fan and M. Graetzel, *Science* 2014, **345**, 1593-1596.
5 J. Low, C. Jiang, B. Cheng, S. Wageh, A. A. Al-Ghamdi, J. Yu, *Small Methods* 2017, **1**, 1700080.
6 N. S. Lewis, *Science* 2016, 351, 353-362.
7 S. Shen, S. A. Lindley, X. Chen and J. Z. Zhang, *Energy Environ. Sci.* 2016, **9**, 2744-2775.
8 F. Ning, M. Shao, S. Xu, Y. Fu, R. Zhang, M. Wei, D. G. Evans and X. Duan, *Energy Environ. Sci.* 2016, **9**, 2633-2643.
9 W. Li, P. Da, Y. Zhang, Y. Wang, X. Lin, X. Gong and G. Zheng, *ACS Nano.* 2014, **8**, 11770-11777.
10 T. W. Kim and K.-S. Choi, *Science*. 2014, **343**, 990-994.
11 S. Kment, F. Riboni, S. Pausova, L. Wang, L. Wang, H. Han, Z. Hubicka, J. Krysa, P. Schmuki and R. Zboril, *Chem. Soc. Rev*. 2017, **46**, 3716-3769.

View Article Online
DOI: 10.1039/C8TA01908H

12 Y. Zhang, H. Zhang, H. Ji, W. Ma, C. Chen and J. Zhao, *J. Am. Chem. Soc*. 2016, **138**, 2705-2711.

13 H. Dotan, O. Kfir, E. Sharlin, O. Blank, M. Gross, I. Dumchin, G. Ankonina and A. Rothschild, *Nat. Mater*. 2013, **12**, 158-164.

14 R. H. Goncalves and E. R. Leite, *Energy Environ. Sci*. 2014, **7**, 2250-2254.

15 S.-S. Yi, J.-M. Yan, B.-R. Wulan, S.-J. Li, K.-H. Liu and Q. Jiang, *Appl. Catal. B: Environ.* 2017, **200**, 477-483.

16 Z. Song, T. Lin, L. Lin, S. Lin, F. Fu, X. Wang and L. Guo, *Angew. Chem. Int. Ed.* 2016, **55**, 2773-2777.

17 F. Nan, Z. Kang, J. Wang, M. Shen, L. Fang, *Appl. Phys. Lett.* 2015, **106**, 153901-153905.

18 J. Liu, Y. Liu, N. Liu, Y. Han, X. Zhang, H. Huang, Y. Lifshitz, S.-T. Lee, J. Zhong and Z. Kang, *Science* 2015, **347**, 970-974.

19 H. Li, Z. Kang, Y. Liu and S.-T. Lee, *J. Mater. Chem.* 2012, **22**, 24230-24253.

20 M. Butler, *J. Appl. Phys.* 1977, **48**, 1914-1920.

21 K.-H. Ye, Z. Wang, J. Gu, S. Xiao, Y. Yuan, Y. Zhu, Y. Zhang, W. Mai and S. Yang, *Energy Environ. Sci.* 2017, **10**, 772-779.

22 X. Zhang, X. Xie, H. Wang, J. Zhang, B. Pan and Y. Xie, *J. Am. Chem. Soc.* 2013, **135**, 18-21.

23 Z. Wang, G. Liu, C. Ding, Z. Chen, F. Zhang, J. Shi and C. Li, *J. Phys. Chem. C* 2015, **119**, 19607-19612.

24 D. Monllor-Satoca, M. Baertsch, C. Fabrega, A. Genc, S. Reinhard, T. Andreu, J. Arbiol, M. Niederberger and J. Ramon Morante, *Energy Environ. Sci.* 2015, **8**, 3242-3254

25 J. Su, Z. Bai, B. Huang, X. Quan and G. Chen, *Nano Energy* 2016, **24**, 148-157.

26 Z. Luo, T. Wang, J. Zhang, C. Li, H. Li and J. Gong, *Angew. Chem. Int. Ed.* 2017, **56**, 12878-12882.

27 P. Zhang, T. Wang, X. Chang, L. Zhang and J. Gong, *Angew. Chem. Int. Ed.* 2016, **55**, 5851-5855.

28 Q. Yu, X. Meng, T. Wang, P. Li and J. Ye, *Adv. Funct. Mater.* 2015, **25**, 2686-2692.

29 Y. Cong, M. Chen, T. Xu, Y. Zhang and Q. Wang, *Appl. Catal. B: Environ.* 2014, **147**, 733-740.

30 P. Peerakiatkhajohn, J.-H. Yun, H. Chen, M. Lyu, T. Butburee and L. Wang, *Adv. Mater.* 2016, **28**, 6405-6410.

31 H. Li, W. Shi, W. Huang, E.-P. Yao, J. Han, Z. Chen, S. Liu, Y. Shen, M. Wang and Y. Yang, *Nano Lett.* 2017, **17**, 2328-2335.

32 X. Chen, Q. Jin, L. Wu, C. Tung and X. Tang, *Angew. Chem. Int. Ed.* 2014, **53**, 12542-12547.

33 J. Zhou, Y. Yang and C.-y. Zhang, *Chem. Commun.* 2013, **49**, 8605-8607.

34 J. Li, Y. Qiu, Z. Wei, Q. Lin, Q. Zhang, K. Yan, H. Chen, S. Xiao, Z. Fan and S. Yang, *Energy Environ. Sci.* 2014, **7**, 3651-3658.

35 C. Du, X. Yang, M. T. Mayer, H. Hoyt, J. Xie, G. McMahon, G. Bischoping and D. Wang, *Angew. Chem. Int. Ed.* 2013, **52**, 12692-12695.

36 P. M. Rao, L. Cai, C. Liu, I. S. Cho, C. H. Lee, J. M. Weisse, P. Yang and X. Zheng, *Nano Lett.* 2014, **14**, 1099-1105.

37 P. S. Bassi, R. P. Antony, P. P. Boix, Y. Fang, J. Barber and L. H. Wong, *Nano Energy*. 2016, **22**, 310-318.

38 S. C. Riha, B. M. Klahr, E. C. Tyo, S. Seifert, S. Vajda, M. J. Pellin, T. W. Hamann and A. B. F. Martinson, *ACS Nano*. 2013, **7**, 2396-2405.

39 Y.-F. Xu, X.-D. Wang, H.-Y. Chen, D.-B. Kuang and C.-Y. Su, *Adv. Funct. Mater*. 2016, **26**, 4414-4421.

40 Y. Hou, F. Zuo, A. P. Dagg, J. Liu and P. Feng, *Adv. Mater.* 2014, **26**, 5043-5049.

41 X. Li, J. Yu, J. Low, Y. Fang, J. Xiao and X. Chen, *J. Mater. Chem. A*. 2015, **3**, 2485-2534.

View Article Online
DOI: 10.1039/C8TA01908H

Table of Contents

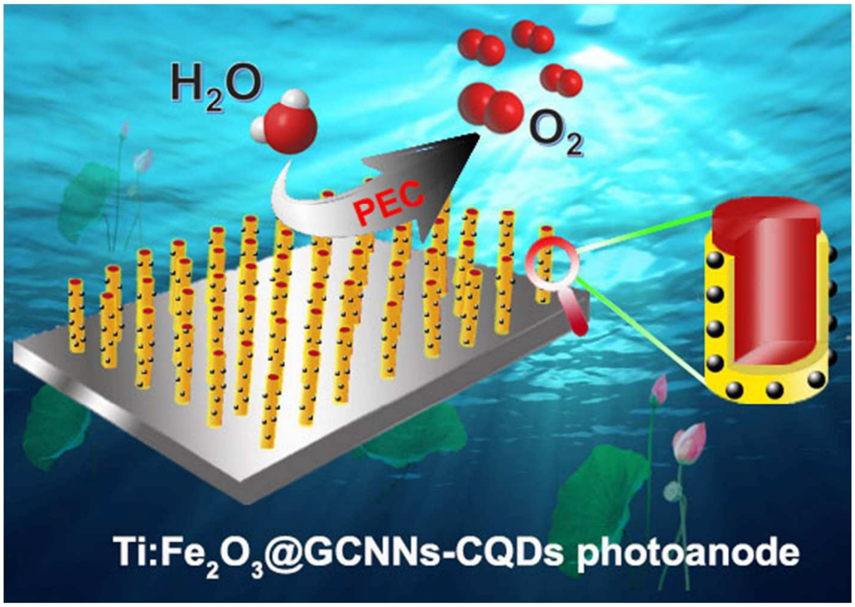

The carbon quantum dots (CQDs) sensitized integrated Ti:Fe_2O_3@g-C_3N_4 core-shell nanoarrays demonstrate superior PEC water oxidation performance can be ascribed to the efficient charge separation efficiency derived from the well-confined heterojunction structure together with the high catalytic activity of CQDs for H_2O_2 via a two-step-two-electron water-splitting process.